IOP PUBLISHING PHYSICA SCRIPTA
Phys. Scr. **T149** (2012) 000000 (8pp) UNCORRECTED PROOF

Numerical simulation of a Richtmyer–Meshkov instability with an adaptive central-upwind sixth-order WENO scheme

V K Tritschler, X Y Hu, S Hickel and N A Adams

Institute of Aerodynamics and Fluid Mechanics, Technische Universität München, 85748 München, Germany

E-mail: volker.tritschler@aer.mw.tum.de

Received 21 February 2012
Accepted for publication 12 May 2012
Published xxx
Online at stacks.iop.org/PhysScr/T149/000000

Abstract
Two-dimensional simulations of the single-mode Richtmyer–Meshkov instability (RMI) are conducted and compared to experimental results of Jacobs and Krivets (2005 *Phys. Fluids* **17** 034105). The employed adaptive central-upwind sixth-order weighted essentially non-oscillatory (WENO) scheme (Hu X Y *et al* 2010 *J. Comput. Phys.* **229** 8952–65) introduces only very small numerical dissipation while preserving the good shock-capturing properties of other standard WENO schemes. Hence, it is well suited for simulations with both small-scale features and strong gradients. A generalized Roe average is proposed to make the multicomponent model of Shyue (1998 *J. Comput. Phys.* **142** 208–42) suitable for high-order accurate reconstruction schemes. A first sequence of single-fluid simulations is conducted and compared to the experiment. We find that the WENO-CU6 method better resolves small-scale structures, leading to earlier symmetry breaking and increased mixing. The first simulation, however, fails to correctly predict the global characteristic structures of the RMI. This is due to a mismatch of the post-shock parameters in single-fluid simulations when the pre-shock states are matched with the experiment. When the post-shock parameters are matched, much better agreement with the experimental data is achieved. In a sequence of multifluid simulations, the uncertainty in the density gradient associated with transition between the fluids is assessed. Thereby the multifluid simulations show a considerable improvement over the single-fluid simulations.

Q1 PACS number: xxx

(Some figures may appear in colour only in the online journal)

1. Introduction

1.1. Richtmyer–Meshkov instability (RMI)

The RMI occurs when the perturbed interface of two fluids with different densities is accelerated impulsively, e.g. by a shock wave [4, 5]. Therefore it is considered as the impulsive limit of the Rayleigh–Taylor instability [6]. The misalignment of the pressure gradient ∇p (associated with the shock wave) and the density gradient $\nabla \rho$ between the two fluids causes baroclinic generation of vorticity on the interface. Baroclinic vorticity deposition is the initial driving force for the development of the primary instabilities. Following the shock passage the disturbances initially present on the interface will grow linearly in time. Nonlinear growth follows when the amplitude of the perturbation becomes important compared to its characteristic wavelength. The nonlinear growth of RMI is characterized by the development of asymmetric 'bubbles' and 'spikes'. Eventually, Kelvin–Helmholtz instability gives rise to the development of small scales. If the initial

energy input is sufficient, a turbulent mixing zone establishes between the fluids where the large-scale structures are progressively broken down into smaller scales. The broadband spectrum of motions present in RMI is one of the main reasons why numerical treatment is challenging. A fundamental understanding of the amplification of initial interface perturbations along with the associated mixing process is of crucial importance for both man-made and natural phenomena. According to Arnett [7], RMI is the reason for the lack of stratification of the supernova 1987a and needs to be taken into account in stellar evolution models. An engineering application of RMI is the strong enhancement of mixing processes, such as the mixing of fuel with an oxidizer in supersonic propulsion engines [8]. A comprehensive description of RMI is given by Brouillette [9] and Zabusky [10] in their reviews.

In recent decades, RMI has been widely studied analytically, numerically and experimentally. In the numerical investigation by Latini *et al* [11, 12], the authors emphasized the importance of high-order reconstruction methods for the simulation of RMI. They found that lower-order methods preserve large-scale structures and symmetry to late times, while higher-order methods could time efficiently resolve small-scale structures, leading to symmetry breaking and increased mixing. This finding that higher-order methods are more time efficient in resolving the broad range of wavelengths present in RMI was one of the motivations to apply the sixth-order adaptive central-upwind weighted essentially non-oscillatory scheme (WENO-CU6) of Hu *et al* [2] to RMI in the present study. Latini *et al* used the experimental study of Collins and Jacobs [13] as the reference. Collins and Jacobs made use of a new technique that allows the development of a defined gas–gas interface without the use of a membrane. This membrane-free technique was first employed by Jones and Jacobs [14]. In the shock-tube experiment of Collins and Jacobs a moderate shock wave interacts with a sinusoidally perturbed material interface of air–acetone. When the shock wave impacts on the interface, baroclinic vorticity production on the interface gives rise to a single-mode RMI. After the first impact the shock wave travels downstream before it is reflected at the end wall of the tube and hits the interface a second time. Later, Jacobs and Krivets [1] used the same experimental setup to redo the experiment at higher Mach numbers. As higher Mach numbers led to faster growth, they were able to obtain valuable information on the late-time development of the single-mode instability, leading to a turbulent mixing zone between the fluids. This experiment is used as the reference in our numerical study.

1.2. Numerical schemes for accelerated compressible multicomponent flows

The broad range of scales present in RMI makes numerical simulations difficult. The numerical discretization method needs to capture steep gradients such as shocks and contact surfaces and should be non-dissipative in smooth flow regions. The RMI is also a multicomponent flow and therefore needs a numerical treatment that is somewhat more complex than for single-component flows. The fluid dynamic properties of multicomponent flows are conventionally modeled by solving additional transport equations for 'information quantities' that account for the presence of different species in the flow. Attempts to attribute conservative properties to these 'information quantities' often suffered from strong unphysical oscillations across the material interface. The occurrence of these numerical inaccuracies led to several publications [15–19] employing non-conservative or quasi-conservative models. In the literature there are also other proposals to maintain pressure equilibrium across material interfaces in a conservative form [20, 21]. Except for Marquina and Pulet's [20] conservative flux-splitting algorithm (they use a conventional WENO-5 reconstruction) all published simulations used low-order reconstruction schemes and effectively fail when combined with a low-dissipation scheme such as WENO-CU6. Some of the proposed models could not properly suppress oscillations when a high-order scheme was applied and some introduced excessive dissipation around the material interface. However, we found the quasi-conservative volume fraction-based model of Abgrall [16], which was later extended from polytropic gases to stiffened gases by Shyue [3], most suitable for use in combination with WENO-CU6. Allaire *et al* [19] generalized the four-equation model of Shyue to a five-equation model that allows the simulation with general equations of state, including tabulated laws. The WENO-CU6 scheme [2] is an attempt to overcome the dissipative nature of other upwind biased WENO schemes; for a review see [22]. WENO-CU6 is based on a new smoothness measure that adapts the numerical stencil between a nonlinear convex combination of lower third-order upwind stencils in regions with steep gradients and a sixth-order central stencil in smooth flow regions. The WENO-CU6 method exhibits enough dissipation close to discontinuities to preserve stability, but allows the stencil to transform to a sixth-order central stencil in smooth flow regions. WENO-CU6 is therefore much less dissipative than other WENO methods. This makes the WENO-CU6 method better suited for direct numerical simulation of RMI with its characteristic broad wavenumber spectrum.

1.3. Scope of the present study

The Euler equations are solved on a two-dimensional (2D) grid. In the computational domain a shock wave first travels through air and then impacts a sinusoidally perturbed interface to SF_6. A single-fluid and a multifluid simulation are conducted and compared to the experiments of Jacobs and Krivets [1]. The aim of this paper is (i) to assess the performance of the WENO-CU6 method for accelerated compressible flows, (ii) to show the importance of using a multicomponent model for the RMI simulation instead of a single-component model, and (iii) to modify the multifluid model such that it ensures pressure equilibrium across the material interface also for high-order methods. Q2

Section 2 presents the governing equations of the problem. Viscous terms are neglected. In section 3, the WENO-CU6 method used for space discretization is outlined together with modifications done to the generalized Roe average of Hu *et al* [23]. These modifications were necessary in order to make the multicomponent model suitable for

the sixth-order method. The initial conditions are discussed in section 5 along with a description of the computational domain in section 5.1 and the non-dimensionalization in section 5.2. The results of both single-component and multicomponent simulations are presented and compared to experiments in section 6, pointing out the importance of a multicomponent model and the use of a low dissipative discretization method for flows where molecular transport plays a weak role. The key findings of this study are then discussed and summarized in section 7.

2. Governing equations

The compressible Euler equations for an ideal binary gas mixture can be written as

$$\frac{\partial \rho}{\partial t} + \nabla \cdot (\rho \boldsymbol{u}) = 0, \tag{2.1}$$

$$\frac{\partial (\rho \boldsymbol{u})}{\partial t} + \nabla \cdot (\rho \boldsymbol{u}\boldsymbol{u} + p\underline{\boldsymbol{\delta}}) = 0, \tag{2.2}$$

$$\frac{\partial E}{\partial t} + \nabla \cdot [(E + p)\boldsymbol{u}] = 0, \tag{2.3}$$

$$\frac{\partial z_{\mathrm{SF}_6}}{\partial t} + \nabla \cdot (\boldsymbol{u} z_{\mathrm{SF}_6}) = z_{\mathrm{SF}_6} \nabla \cdot \boldsymbol{u}, \tag{2.4}$$

where ρ is the mixture density, $\boldsymbol{u}$ is the velocity, p is the pressure, E is the total energy, z_{SF_6} is the volume fraction of SF_6 gas and $\underline{\boldsymbol{\delta}}$ is the unit tensor. The volume fraction of air is easily obtained by $z_{\mathrm{air}} = 1 - z_{\mathrm{SF}_6}$. The equations are closed with the equation of state (EOS) for an ideal gas

$$p(\rho e, z) = (\overline{\gamma}(z) - 1)\rho e, \tag{2.5}$$

where $\overline{\gamma}$ is the ratio of specific heats of the gas mixture with [3]

$$\frac{1}{\overline{\gamma} - 1} = \sum_i \frac{z_i}{\gamma_i - 1}. \tag{2.6}$$

The internal energy of the system is denoted as e and is defined as

$$e = \frac{E}{\rho} - \frac{1}{2}\boldsymbol{u}^2. \tag{2.7}$$

3. Numerical scheme

In the 1D case, system (2.1)–(2.3) can be written in the conservative form as

$$\boldsymbol{U}_t + \boldsymbol{F}(\boldsymbol{U})_x = 0 \tag{3.1}$$

with $\boldsymbol{U} = (\rho, \rho u, E)^{\mathrm{T}}$ and $\boldsymbol{F}(\boldsymbol{U}) = (\rho u, p + \rho u^2, u(E + p))^{\mathrm{T}}$.

We solve (3.1) in characteristic form. The eigensystem of fluxes in (3.1) is obtained from the Roe-averaged Jacobian, which yields the left and right eigenvectors. The left eigenvectors project the fluxes onto the characteristic field, and the eigenvalues of the Jacobian are used to ensure upwinding.

To obtain high-order accurate numerical fluxes at the cell boundaries $\hat{f}_{i\pm1/2}$, the WENO-CU6 method is employed to reconstruct these values from cell averages. Finally, the reconstructed numerical fluxes at the cell face are projected back onto the physical field using the right eigenvectors. An entropy fix is implemented by the Lax–Friedrichs flux splitting. For more details of Riemann solvers, see [24]. The left-hand side of (3.1) is evolved in time using a third-order total variation diminishing Runge–Kutta scheme.

3.1. The adaptive central-upwind sixth-order WENO scheme

The motivation for Hu *et al* [2] to develop the WENO-CU6 discretization scheme was that standard WENO schemes exhibit excessive dissipation and accordingly overwhelm large amounts of the small-scale structure in a flow. The principle of the WENO-CU6 method is to use a non-dissipative sixth-order central method in smooth flow regions and a nonlinear convex combination of third-order approximation polynomials in regions with steep gradients. This new weighting strategy preserves the good shock capturing properties of other WENO methods, while it can achieve very low numerical dissipation in smooth flow regions.

The reconstructed numerical fluxes at the cell boundaries are computed from

$$\hat{f}_{i+1/2} = \sum_{k=0}^{3} \omega_k \hat{f}_{k,i+1/2}, \tag{3.2}$$

where ω_k is the weight assigned to stencil k with the second-degree reconstruction polynomial approximation $\hat{f}_{k,i+1/2}$. In the WENO-CU6 framework the weights ω_k are given by

$$\omega_k = \frac{\alpha_k}{\sum_{k=0}^{3} \alpha_k}, \quad \alpha_k = d_k \left(C + \frac{\tau_6}{\beta_k + \epsilon} \right). \tag{3.3}$$

The optimal weights d_k are chosen such that the method recovers the sixth-order central method. C is a constant with $C \gg 1$. A new smoothness measure τ_6 can be found from a linear combination of the other smoothness measures β_k with

$$\tau_6 = \beta_6 - \frac{1}{6}(\beta_0 + \beta_2 + 4\beta_1) \tag{3.4}$$

and

$$\beta_k = \sum_{j=0}^{2} \Delta x^{2j-1} \int_{x-1/2}^{x_{i+1/2}} \left(\frac{\mathrm{d}^j}{\mathrm{d}x^j} \hat{f}_k(x) \right)^2 \mathrm{d}x. \tag{3.5}$$

β_6 is also calculated from (3.5) but with the six-point stencil for the sixth-order interpolation. The full method is given in [2] and with modifications for scale separation in [25].

3.2. The modified general Roe average for an ideal gas mixture

The general Roe average used in the present study is an extension of the Roe average for generalized EOS, but unlike those of Liou *et al* [26] and Shyue [27], the method is simple and satisfies the U-property exactly. Moreover, it does not introduce artificial states like that of Glaister [28] and predicts the averages directly from the adjacent states.

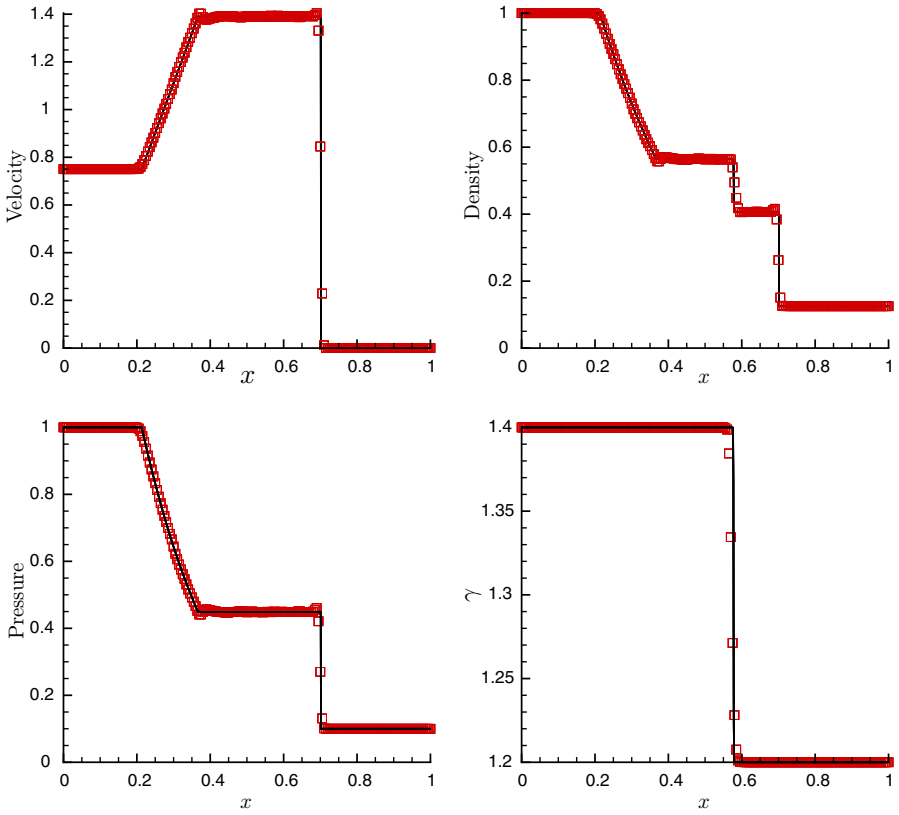

Figure 1. Results of Sod's two-material shock-tube problem for the WENO-CU6 scheme (□) on a 200-point grid compared to the reference solution (—) obtained with the WENO-5 scheme on a high-resolution 6000-point grid.

Here we apply this method with the Riemann solver of Roe. Additional challenges arise from the fact that the linear approximation between the average state and the adjacent state for a single-phase interaction, which has been assumed by Hu *et al* [23], does not hold in the present study.

According to Glaister [28], the averages of $\tilde{\rho}$, $\tilde{u}$ and $\tilde{H}$ can be obtained from

$$\tilde{\rho} = \sqrt{\rho_\mathrm{l}\rho_\mathrm{r}}, \quad \tilde{f} = \mu(f) = \frac{\sqrt{\rho_\mathrm{l}} f_\mathrm{l} + \sqrt{\rho_\mathrm{r}} f_\mathrm{r}}{\sqrt{\rho_\mathrm{l}} + \sqrt{\rho_\mathrm{r}}}, \quad f = u, H \tag{3.6}$$

and

$$\left(\frac{\tilde{p}}{\rho}\right) = \mu\left(\frac{p}{\rho}\right) + \frac{\tilde{\rho}}{2}\left(\frac{u_\mathrm{r} - u_\mathrm{l}}{\sqrt{\rho_\mathrm{l}} + \sqrt{\rho_\mathrm{r}}}\right)^2. \tag{3.7}$$

The average pressure can be evaluated from (3.7) as $\tilde{p} = \tilde{\rho}(\frac{\tilde{p}}{\rho})$. For a general EOS $p = p(\rho, e)$, the speed of sound c is given by

$$c^2 = \left.\frac{\partial p}{\partial \rho}\right|_e + \frac{p}{\rho^2}\left.\frac{\partial p}{\partial e}\right|_\rho = \Psi + \Gamma\frac{p}{\rho}, \tag{3.8}$$

where Ψ is the Grüneisen coefficient and Γ defines the material properties. Following Roe [29] and Glaister's [28] approach, one obtains the condition for the pressure difference between two adjacent states as

$$\Delta p = \tilde{\Psi}\Delta\rho + \tilde{\Gamma}[\Delta(\rho e) - \tilde{e}\Delta\rho] \tag{3.9}$$

with appropriately defined average states for the Grüneisen coefficient $\tilde{\Psi}$ and the parameter defining the material properties $\tilde{\Gamma}$.

Unlike Hu *et al* [23], we cannot assume a linear approximation between the average and the adjacent states, which would reduce the equation for the pressure difference (3.9) to

$$\Delta p = \tilde{\Psi}\Delta\rho + \tilde{\Gamma}\tilde{\rho}\Delta e, \tag{3.10}$$

but we need to find the averages $\tilde{\Psi}$ and $\tilde{\Gamma}$ based on (3.9).

One way to calculate $\tilde{\Psi}$ and $\tilde{\Gamma}$ is to assume that one of them obeys the same averaging as $\tilde{f}$ in (3.6) and calculate the other one from (3.9). This would lead to

$$\tilde{\Gamma}_{\Delta e} = \frac{\Delta p - \mu(\Psi)\Delta\rho}{\Delta(\rho e) - \tilde{e}\Delta\rho} \tag{3.11}$$

and

$$\tilde{\Psi}_{\Delta\rho} = \frac{\Delta p - \mu(\Gamma)[\Delta(\rho e) - \tilde{e}\Delta\rho]}{\Delta\rho}, \tag{3.12}$$

respectively. The averaged internal energy for an ideal gas can be found as

$$\tilde{e} = \frac{\mu(\Psi)}{\mu(\Gamma)}. \tag{3.13}$$

However, (3.11) and (3.12) are undefined if $\Delta(\rho e) - \tilde{e}\Delta\rho = 0$ or $\Delta\rho = 0$. The singularities can be removed if it is assumed that $\tilde{\Gamma} = \mu(\Gamma)$ when $\Delta(\rho e) - \tilde{e}\Delta\rho = 0$ and $\tilde{\Psi} = \mu(\Psi)$ when $\Delta\rho = 0$. Thus the modified generalized definitions of $\tilde{\Gamma}$ and $\tilde{\Psi}$ can be expressed as

$$\tilde{\Gamma} = \frac{\mu(\Psi)(w_e + \epsilon) + \tilde{\Psi}_{\Delta\rho} w_\rho}{w_e + w_\rho + \epsilon}, \quad \tilde{\Psi} = \frac{\mu(\Gamma)(w_\rho + \epsilon) + \tilde{\Gamma}_{\Delta e} w_e}{w_e + w_\rho + \epsilon} \tag{3.14}$$

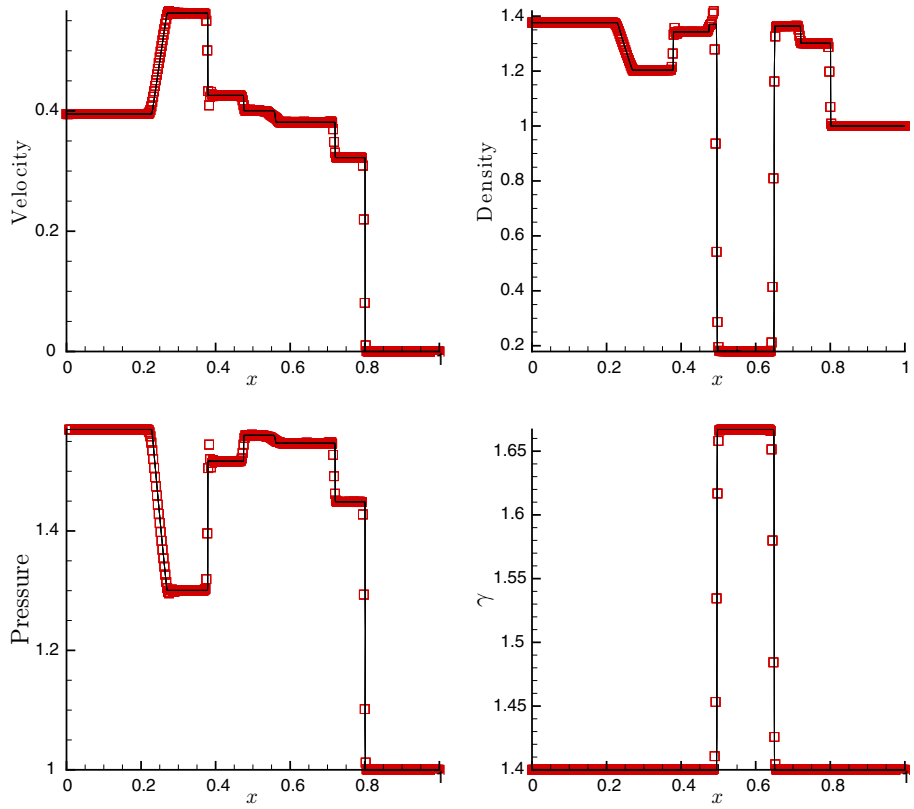

Figure 2. Results of the 1D shock–bubble interaction test case of Quirk and Karni. The WENO-CU6 solution (□) is obtained on a 400-point grid and compared to the reference solution (—) produced with the standard WENO-5 method on a high-resolution grid with 6000 grid points.

with $w_\rho = (\frac{\Delta\rho}{\tilde{\rho}})^2$ and $w_e = (\frac{\Delta(\rho e) - \tilde{e}\Delta\rho}{\tilde{\rho}\tilde{e}})^2$, where ϵ is a small number. Then the speed of sound is given by

$$c^2 = \tilde{\Psi} + \frac{\tilde{p}}{\tilde{\rho}}\tilde{\Gamma}. \tag{3.15}$$

4. Validation of the numerical scheme

As a first validation test case, Sod's two-material shock-tube problem is used to show the correct and consistent implementation of the WENO-CU6 scheme and the multicomponent model with its modified generalized Roe average. The initial condition is

$$(\rho, u, p, \gamma) = \begin{cases} (1.0, 0.75, 1.0, 1.4) & \text{if} \quad 0.0 < x < 0.3, \\ (0.125, 0.0, 0.1, 1.2) & \text{if} \quad 0.3 < x < 1.0. \end{cases} \tag{4.1}$$

Results are shown for the final time $t = 0.2$.

The solution in figure 1 obtained with the WENO-CU6 scheme on a 200-point grid agrees very well with the reference solution. The reference solution is produced with a standard WENO-5 scheme on a high-resolution grid with 6000 points. The results of the WENO-CU6 method slightly oscillate because of the non-dissipative properties of the method. A more dissipative scheme would damp such disturbances at each time step and hence smooth out the solution. In a non-dissipative scheme (as the WENO-CU6 scheme is in smooth flow regions) the oscillations show a dispersive character as they travel both up- and downstream.

The second test case is the 1D shock–bubble interaction case of Quirk and Karni (cited by Abgrall [16]). It consists of a shock wave that is traveling in air to the right. In the pre-shock state a bubble of helium is located between $0.4 < x < 0.6$. The shock wave is initially at $x = 0.25$ and the initial conditions are

$$(\rho, u, p, \gamma) = \begin{cases} (1.3765, 0.3948, 1.57, 1.4) & \text{if} \quad 0.0 < x < 0.25, \\ (1.0, 0.0, 1.0, 1.4) & \text{if} \quad 0.25 < x < 0.4 \\ & \quad \text{or} \quad 0.6 < x < 1.0, \\ (0.138, 0.0, 1.0, 1.67) & \text{if} \quad 0.4 < x < 0.6. \end{cases} \tag{4.2}$$

The results of the WENO-CU6 method are given in figure 2 and compared to the reference solution that was obtained by using a conventional WENO-5 approach. The solution of the WENO-CU6 method was sampled on a 400-point grid. The reference solution was sampled on a high-resolution 6000-point grid. Although the WENO-CU6 results were obtained on a grid that is 15 coarser than the grid of the reference solution, they are both in very good agreement. A quantitative comparison of the present results with those of Wang [21] showed a clear improvement. Also a qualitative comparison with the results of Marquina and Pulet [20] corroborated this conclusion.

5. Initial conditions for RMI

The experiments of Jacobs and Krivets [1] provide the initial conditions for our 2D investigation of the RMI in an inviscid

regime. The vertical shock tube used in the experiment has a driver section that is filled with air at ambient pressure and temperature. In the test section an interface of air–SF_6 is formed as the heavier SF_6 flows upwards and collides with air flowing from top to down. Both gases exit through horizontal slots in the test section. A sinusoidal interface between the two gases is formed by oscillating the entire shock tube in the horizontal direction. This membrane-less technique was first proposed by Jones and Jacobs [14].

The initial conditions of the experimental setup considered in the present numerical study are as follows: The shock wave has a strength of $M_s = 1.3$ in air. The sinusoidal interface of air–SF_6 has a pre-shock amplitude of $a_0^- = 2.9\,\text{mm}$ and a wavelength of $\lambda = 59\,\text{mm}$. The location of the material interface is then calculated from $\eta = x_i + a_0^- \cos(2\pi y)$. The diffusion layer between the fluids is given by [30]

$$f(\delta) = f_1(1-\delta) + f_r\delta,$$
$$\delta = \frac{(1+\tanh(\frac{\Delta R}{\epsilon}))}{2}, \qquad (5.1)$$
$$\epsilon = D\sqrt{\Delta x_i \Delta y_i}$$

and $f = \rho, z_{SF_6}$. ΔR is the distance from the material interface. The densities of air and SF_6 in ambient conditions led to a pre-shock Atwood number of $A^- = 0.605$. The interface is initialized at $x_I = 30\,\text{mm}$ and the shock at $x_s = 10\,\text{mm}$. The time is initialized to zero ($t = 0$) when the shock first impacts the SF_6 gas.

5.1. Computational domain

The 2D computational domain is discretized by a Cartesian grid. We use for all simulations a mesh size of 256 cells per initial wavelength λ. The 'numerical test section' is surrounded by layers of coarser grids in order to avoid shock reflections at the inlet and outlet.

5.2. Non-dimensionalization

The reference scales to non-dimensionalize the governing equations are defined here. The reference density is set to the pre-shock density of air $\rho_{ref} = \rho_{air} = 1.351\,\text{kg m}^{-3}$. Accordingly, the reference pressure is chosen to be the pre-shock pressure $p_{ref} = 0.956$ bar. The reference length scale is the initial wavelength of the sinusoidal interface $L_{ref} = \lambda = 59\,\text{mm}$ and the reference time scale is $t_{ref} = \sqrt{\frac{\rho_{ref}}{p_{ref}}} L_{ref}$.

6. Numerical results

6.1. Single-fluid algorithm

In this subsection, the ratio of specific heats $\overline{\gamma}$ in (2.5) is assumed to be constant with the same value of $\overline{\gamma} = 1.276$ for both air and SF_6 and hence is referred to as single-fluid algorithm. Figure 3 shows the experimental results of Jacobs and Krivets [1] along with our numerical results obtained with the standard WENO-5 and the WENO-CU6 method at three different times $t = 3.06\,\text{ms}$, $t = 4.16\,\text{ms}$ and $t = 6.06\,\text{ms}$.

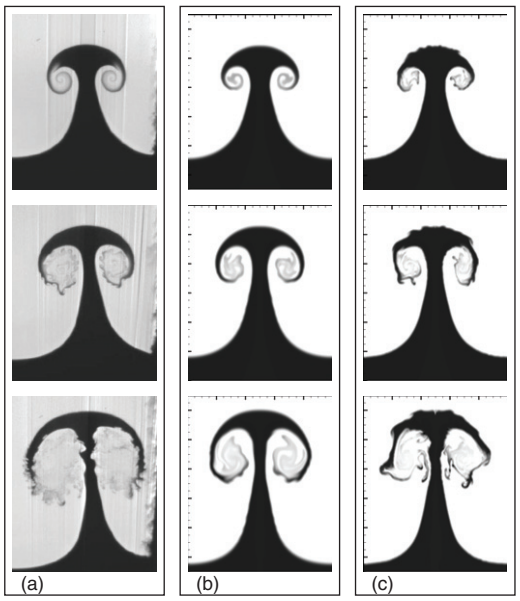

Figure 3. Experimental results of Jacobs and Krivets [1] (a) compared to the single-fluid results obtained with the standard WENO-5 method (b) and the WENO-CU6 method (c) at three different times $t = 3.06\,\text{ms}$, $t = 4.16\,\text{ms}$ and $t = 6.06\,\text{ms}$.

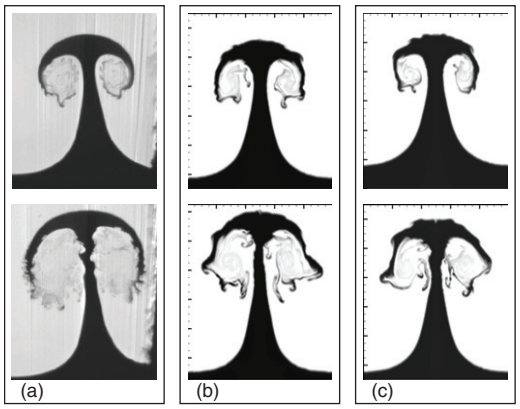

Figure 4. In (b) the post-shock conditions of the experiment are matched, whereas in (c) the pre-shock conditions are matched and compared to the experiment (a) at times $t = 4.16\,\text{ms}$ and $t = 6.06\,\text{ms}$.

The comparison shows that the lower-order WENO-5 method preserves large-scale structures and symmetry to later times, while WENO-CU6 better resolves small-scale structures, leading to symmetry breaking and increased mixing. This better behavior is in agreement with the findings of Latini *et al* [11].

WENO-5 cannot reproduce the secondary instabilities on the mushroom stem, whereas WENO-CU6 clearly shows the same typical stem disturbances as the experiment at $t = 6.06\,\text{ms}$. On the other hand, it also shows instabilities on top of the mushroom which are not observed in the experiment. We believe that the origin of these numerical instabilities could be because of neglecting viscous effects, which makes the WENO-CU6 scheme less dissipative than the real physical mechanisms. On the other hand, other numerical schemes apparently are too dissipative. Both discretization schemes are unable to predict correctly the large-scale structure such

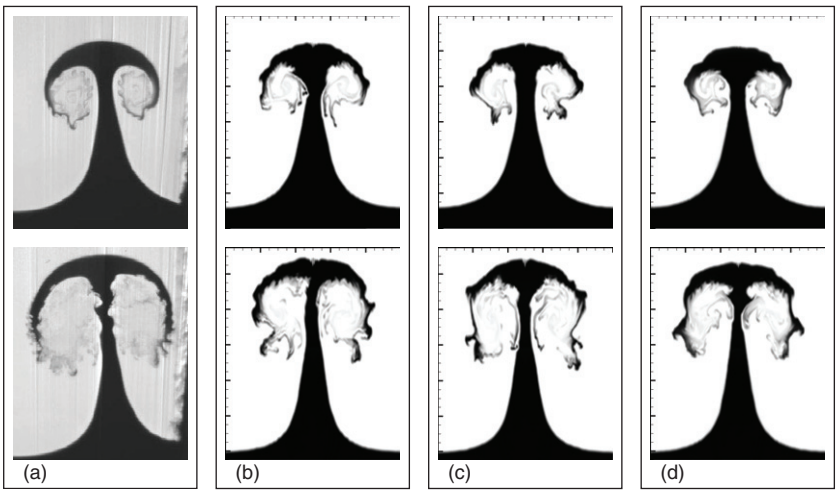

Figure 5. Investigation of the impact of the diffusion layer on the late-time Richtmyer–Meshkov development with increasing the diffusion layer thickness from (b) $D = 4$ to (c) $D = 8$ to (d) $D = 16$ at times $t = 4.16$ ms and $t = 6.06$ ms.

as the mushroom head diameter and stem diameter of the RMI experiment.

Richtmyer described the early linear growth rate of the instability as a function of the post-shock parameters, a_0^+ the post-shock amplitude, A^+ the post-shock Atwood number, the velocity jump ΔU_0 associated with the shock passage and k the initial perturbation wavelength

$$ka(t) = ka_0^+ + k^2 a_0^+ A^+ \Delta U_0 t. \tag{6.1}$$

From (6.1) it immediately follows that in order to match the correct initial growth rate and accordingly the later development, one needs to reproduce the correct post-shock parameters. As the single-fluid method assumes constant $\overline{\gamma}$, it is not possible to have matching pre- and post-shock states. Thus, it is preferable to match the post-shock state in order to improve the agreement in the large-scale structures between
Q5 experiments and numerics at late times.

In figure 4(b), the post-shock parameters are matched and compared to the results where the pre-shock states
Q6 are matched (figure 4(c)). Comparing figures 4(a)–(c), we observe a clear improvement of the large-scale structures, as figure 4(b) shows a wider mushroom head and a thinner stem, which captures better the global characteristics of the RMI experiments.

6.2. Multifluid algorithm

In this subsection, $\overline{\gamma}$ is not assumed to be constant but computed from (2.6) with $\gamma_{\text{air}} = 1.276$ and $\gamma_{\text{SF}_6} = 1.093$. A transport equation is solved for the volume fraction (2.4) to account for the variable ratio of specific heats. By means of (2.4) and the modified general Roe average of section 3.2 we are able to simulate the material interface without the appearance of spurious pressure oscillations.

As the initial driving force of RMI is the vorticity deposition on the material interface caused by the misaligned pressure and density gradient, it is of crucial importance to properly match the pressure gradient and the density gradient. The pressure gradient is associated with the Mach number of the incident shock wave and therefore is much better quantifiable than the density gradient.

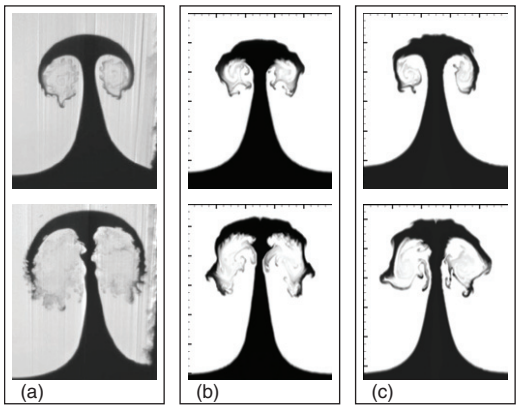

Figure 6. Comparison of the multifluid (b) and single-fluid (c) algorithms to the experiments (a) at times $t = 4.16$ ms and $t = 6.06$ ms.

In order to quantify the uncertainty of the density distribution across the interface, three different diffusion layer thicknesses are considered. Figure 5 shows a sequence of simulations with increasing diffusion layer thicknesses $D = 4$, $D = 8$ and $D = 16$, see (5.1). The vorticity deposited on the interface decreases as the density gradient is reduced from the left, figure 5(b), to the right, figure 5(d). Although the mushroom stem in figure 5(d) shows a non-sinusoidal perturbation the overall shape agrees best with the experiment. $D = 16$ is therefore used for making a comparison to the results obtained using WENO-CU6 and a constant ratio of specific heats in figure 6.

Figure 6 reveals a clear improvement of the multifluid algorithm over the single-fluid algorithm. The global characteristics are captured much better in figure 6(b) than in figure 6(c). When the late-time development of the RMI is of interest the correct compressibility of the fluids involved needs to be captured, which requires a multifluid simulation with variable material properties.

7. Concluding remarks

The 2D simulations of the single-mode RMI using the recently developed WENO-CU6 reconstruction method of Hu *et al* [2]

were conducted and compared with the experiments of Jacobs and Krivets [1]. The multicomponent model for stiffened gases by Shyue [3] was used to account for multiple species. However, the high-order method employed made it necessary to modify the general Roe average of Hu *et al* [23] in order to capture material interfaces without the occurrence of spurious pressure oscillations. In two 1D test cases it was shown that the WENO-CU6 method together with the modified general Roe average was capable of capturing accurately material interfaces without introducing undesirable amounts of numerical dissipation.

In a first sequence of simulations the ratio of specific heats $\overline{\gamma}$ was assumed to be constant for both fluids. The fluxes were reconstructed with the WENO-CU6 and the standard WENO-5 method and compared to the experiments. It was concluded that the lower-order WENO-5 method preserves large-scale structures and symmetry to later times, while the WENO-CU6 better resolves small-scale structures, leading to earlier symmetry breaking and increased mixing. This better behavior is in agreement with the findings of Latini *et al* [11]. However, the global characteristic structures of RMI were matched neither by the WENO-CU6 method nor by the WENO-5 method. This is due to the fact that the linear growth rate of RMI essentially depends on the post-shock state of the instability. A mismatch of the post-shock state essentially leads to wrong prediction of the late-time development. Thus, in terms of accuracy, it is much more preferable to match the post-shock state than the pre-shock state in single-fluid simulations.

The initial driving force of RMI is the vorticity deposition on the material interface caused by the non-parallel pressure and density gradient. However, unlike the pressure gradient, the density gradient associated with the material interface is not easy to quantify in experiments. Therefore, a sequence of multifluid simulations with different diffusion layer thicknesses were conducted to assess the uncertainty in the density gradient. The multifluid simulations showed a considerable improvement over the single-fluid simulations where the pre-shock state is matched.

Acknowledgments

VKT is a member of the TUM Graduate School and acknowledges the support he received.

References

[1] Jacobs J W and Krivets V V 2005 Experiments on the late-time development of single-mode Richtmyer–Meshkov instability *Phys. Fluids* **17** 034105
[2] Hu X Y, Wang Q and Adams N A 2010 An adaptive central-upwind weighted essentially non-oscillatory scheme *J. Comput. Phys.* **229** 8952–65
[3] Shyue K-M 1998 An efficient shock-capturing algorithm for compressible multicomponent problems *J. Comput. Phys.* **142** 208–42
[4] Richtmyer R D 1960 Taylor instability in shock acceleration of compressible fluids *Commun. Pure Appl. Math.* **XIII** 297–319
[5] Meshkov E E 1969 Instability of the interface of two gases accelerated by a shock wave *Fluid Dyn.* **4**
[6] Taylor G I 1950 The instability of liquid surfaces when accelerated in a direction perpendicular to their planes *Proc. R. Soc.* A **201** 192
[7] Arnett D 2000 The role of mixing in astrophysics *Appl. J. Suppl.* **127** 213–17
[8] Yang J, Kubota T and Zukoski E E 1993 Applications of shock-induced mixing to supersonic combustion *AIAA J.* **31** 854–62
[9] Brouillette M 2002 The Richtmyer-Meshkov instability *Annu. Rev. Fluid Mech.* **34** 445–68
[10] Zabusky N 1999 Vortex paradigm for accelerated inhomogenous flows: visiometrics for the Rayleigh–Taylor and Richtmyer–Meshkov environments *Annu. Rev. Fluid Mech.* **31** 495
[11] Latini M, Schilling O and Don W S 2007 Effects of WENO flux reconstruction order and spatial resolution on reshocked two-dimensional Richtmyer–Meshkov instability *J. Comput. Phys.* **221** 805–36
[12] Latini M, Schilling O and Don W S 2007 High-resolution simulations and modeling of reshocked single-mode Richtmyer–Meshkov instability: comparison to experimental data and to amplitude growth model predictions *Phys. Fluids* **19** 024104
[13] Collins B D and Jacobs J W 2002 PLIF flow visualization and measurements of the Richtmyer–Meshkov instability of an air/SF_6 interface *J. Fluid Mech.* **464** 113–36
[14] Jones M A and Jacobs J W 1997 A membraneless experiment for the study of Richtmyer–Meshkov instability of a shock-accelerated gas interface *Phys. Fluids* **9** 3078–85
[15] Karni S 1994 Multicomponent flow calculations by a consistent primitive algorithm *J. Comput. Phys.* **112** 31–43
[16] Abgrall R 1996 How to prevent pressure oscillations in multicomponent flow calculations: a quasi conservative approach *J. Comput. Phys.* **125** 150–60
[17] Karni S 1996 Hybrid multifluid algorithms *SIAM J. Sci. Comput.* **17** 1019
[18] Abgrall R 2001 Computations of compressible multifluids *J. Comput. Phys.* **169** 594–623
[19] Allaire G, Clerc S and Kokh S 2002 A five equation model for the simulation of the interface between compressible fluids *J. Comput. Phys.* **181** 577–616
[20] Marquina A and Pulet P 2003 A flux-split algorithm applied to conservative models for multicomponent compressible flows *J. Comput. Phys.* **185** 120–38
[21] Wang S 2004 A thermodynamically consistent and fully conservative treatment of contact discontinuities for compressible multicomponent flows *J. Comput. Phys.* **195** 528–59
[22] Shu C-W 1997 Essentially non-oscillatory and weighted essentially non-oscillatory schemes for hyperbolic conservation laws *ICASE Report* no. 97-65
[23] Hu X Y, Adams N A and Iaccarino G 2009 On the HLLC Riemann solver for interface interaction in compressible multi-fluid flow *J. Comput. Phys.* **228** 6572–89
[24] Toro E F 1999 *Riemann Solvers and Numerical Methods for Fluid Dynamics* (Berlin: Springer)
[25] Hu X Y and Adams N A 2011 Scale separation for implicit large eddy simulation *J. Comput. Phys.* **230**
[26] Liou M S, B van Leer and Shuen J S 1990 Splitting for inviscid fluces for real gas *J. Comput. Phys.* **87** 1–24
[27] Shyue K M 2001 A fluid-mixture type algorithm for compressible multicomponent flow with Mie–Gruneisen equation of state *J. Comput. Phys.* **171** 678–707
[28] Glaister P 1988 An approximate linearised Riemann solver for the Euler equations for real gases *J. Comput. Phys.* **74** 382–408
[29] Roe P L 1981 Approximate Riemann solvers, parameter and difference schemes *J. Comput. Phys.* **43** 357–72
[30] Shankar S K, Kawai S and Lele S K 2010 Numerical simulation of multicomponent shock accelerated flows and mixing using localized artificial diffusivity method *4th AIAA Aerospace Science Meeting*

QUERY FORM

JOURNAL: ps

AUTHOR: V K Tritschler *et al*

TITLE: Numerical simulation of a Richtmyer–Meshkov instability with an adaptive central-upwind sixth-order WENO scheme

ARTICLE ID: pstop437193

Page 1

Q1.
Author: Please provide the PACS numbers.

Page 2

Q2.
Author: Please verify the changes in the sentence 'The aim of . . . methods'.

Page 3

Q3.
Author: Please check the changes in the sentence 'The results of . . . role'.

Q4.
Author: Please check 'Closed with' in the sentence 'The equations . . . (2.6)'.

Page 7

Q5.
Author: Please check the changes in the sentence 'Thus, . . . late-times'.

Q6.
Author: Please check the sentence 'In figure 4(b) . . . 4(c)' for clarity.

Page 8

Q7.
Author: Please check the details for any journal references that do not have a blue link as they may contain some incorrect information. Pale purple links are used for references to arXiv e-prints.

Q8.
Author: Please provide page number in [5, 25].

Q9.
Author: Please provide page number in [30].

Author: please be aware that the colour figures in this article will only appear in colour in the Web version. If you require colour in the printed journal and have not previously arranged it, please contact the Production Editor now.